

ASSESSMENT OF RESERVOIR PROCESSES INDUCED BY GEOTHERMAL UTILIZATION AT REYKJANES, SW-ICELAND, INFERRED FROM INTERFEROMETRIC ANALYSIS OF SATELLITE IMAGES AND GNSS GEODESY 2005-2019

Mylene Receveur^{*1,2}, Freysteinn Sigmundsson¹, Michelle Parks³, Vincent Drouin⁴, Halldor Geirsson¹, Sigrun Hreinsdottir⁵, Omar Sigurdsson⁶

¹Nordic Volcanological Center, Institute of Earth Sciences, University of Iceland, Reykjavik, Iceland

²Now at: School of Geosciences, University of Edinburgh, Edinburgh, Scotland

³Icelandic Meteorological Office, 150 Reykjavik, Iceland

⁴Iceland GeoSurvey, Grensásvegi 9, 108 Reykjavík, Iceland

⁵GNSScience, Lower Hutt, New Zealand

⁶HSOrka, Grindavík, Iceland

^{*}E-mail address: M.Receveur@sms.ed.ac.uk

Keywords: High-temperature geothermal system, Radar interferometry, Time-series analysis; Ground deformation modeling; Steam zone

ABSTRACT

We study local deformation induced by geothermal utilization of the high-temperature Reykjanes system, SW-Iceland, since 2006 when a new 100 MWe power plant began operation. Using interferometric analyses of synthetic aperture radar (InSAR) of images acquired by the Sentinel-1 satellites, we provide an update of the time series of surface displacement above the geothermal reservoir for the 2015-2019 time period. Results from previous studies showed that the highest rates were observed for the 2005-2008 period, where the main deformation area was aligned along the Reykjanes fissure swarm in the vicinity of the power plant. From 2009, the deformation zone narrowed to a 2-km wide circular subsidence bowl centered on the well field accompanied by a decrease in the maximum subsidence rate. The decrease in the rate of volume change together with the migration of the best-fitting source toward shallower depth between the 2005–2008 and 2009-2019 periods was attributed to a change in the deformation processes within the reservoir. While deformation in the 2005-2008 period was related to the compaction of deep rocks as a result of a 3 MPa pressure drop in the initial years of geothermal production, the continuous subsidence since 2009 was attributed to a combination of both poro- and thermo-elastic compaction within or near a steam zone, formed in the topmost part of the reservoir in response to this pressure drop. Time-series of range change in the satellite line-of-sight (LOS) for the 2015-2019 period confirm the continuous deflation in the area of maximum geothermal utilization, at an increased rate during the 2018-2019 interval. A total subsidence of about 330 mm together with horizontal contraction towards the center of deflation of up to about 170 mm is inferred for the 2006-2019 period. The average ascending and descending LOS velocities are used to invert for the characteristics of the deformation source for the 2015-2019 and 2018-2019 time periods, modeling the reservoir as a body of simple geometry within an elastic half space. Results for both periods indicate a best-fitting source at ~1.4 km depth contracting at a rate of about $-0.9 \times 10^5 \text{ m}^3 \text{ yr}^{-1}$. This is comparable to values found since 2006, despite the higher deformation rates in the central area of deformation. Pressure measurements in boreholes since the end of 2017 indicate renewed pressure decline at 1.6 km depth that correlates well with the increase rate of subsidence and contraction rates observed in the center of the deformation field since 2018. However, we suggest that more time and further work is necessary for the effects of this pressure drop to reach the surface and to be able to determinate more precisely the characteristics of the deformation source from 2018, through inverse modeling of geodetic data.

1. INTRODUCTION

Since the 1990, Interferometric Synthetic Aperture Radar (InSAR) satellite imaging methods have been increasingly used to study ground deformation induced by geothermal utilization. The combined use of GPS-Geodesy and InSAR has proven to be an efficient tool to monitor long-term changes within geothermal reservoirs. We here undertake an extended interferometric analysis of Sentinel-1 images acquired between 2017 and 2019 at the Reykjanes geothermal system, SW-Iceland, and integrate the result into the long-term deformation history provided by studies from Parks *et al.* (2018) and Receveur *et al.* (2019) to understand changes in the reservoir resulting from geothermal utilization in this area.

The high-temperature Reykjanes geothermal system (Fig. 1) is located where the Mid-Atlantic Ridge emerges on the southwestern tip of the Reykjanes Peninsula in Iceland (Bjornsson *et al.*, 1970). The geological structure consists of a highly fractured superimposition of volcano-sedimentary strata and subaerial Pleistocene lava flows (Friðleifsson *et al.*, 2014). The upper part of the series is dominated by phreato-magmatic tuffs and breccias intersected by thin layer of fossiliferous marine sediments, mainly found between 400 and 800 m depth (Friðleifsson and Richter 2010). Below 1100 m depth, the sequence is dominated by crystalline pillow basalts and breccias formed in deep-water environments. An increasing density of dyke intrusions are encountered in wells below 1.5 km depth, and they dominate the sequence from 2.8 km depth (Franzson 2004). The geothermal reservoir is bounded by two main faults channeling recharge from the SW and forming a NE/Ene graben structure. The highest temperatures at 1 km depth were measured in well RN-10, situated in the central part of this graben (Franzson *et al.*, 2002). On surface, an area of intense hydrothermal activity of about 2 km² has been used to delineate the central part of the reservoir, where the permeability and temperatures are the

highest (Fridriksson *et al.*, 2010). Assuming a thickness of 1500 m, the total volume of the productive reservoir was estimated to be approximately 3 km³. Some productive layers have been identified within porous formations at 800–1200 m depth, below the highly altered reservoir cap rock located in the 400–900 m depth range (Friðleifsson *et al.*, 2014). However, most of the feed zones are fracture-related and irregularly distributed within the reservoir, the largest ones being associated with sub-vertical fractures along or near dykes between 1.9 and 2.3 km depth (Franzson *et al.*, 2002).

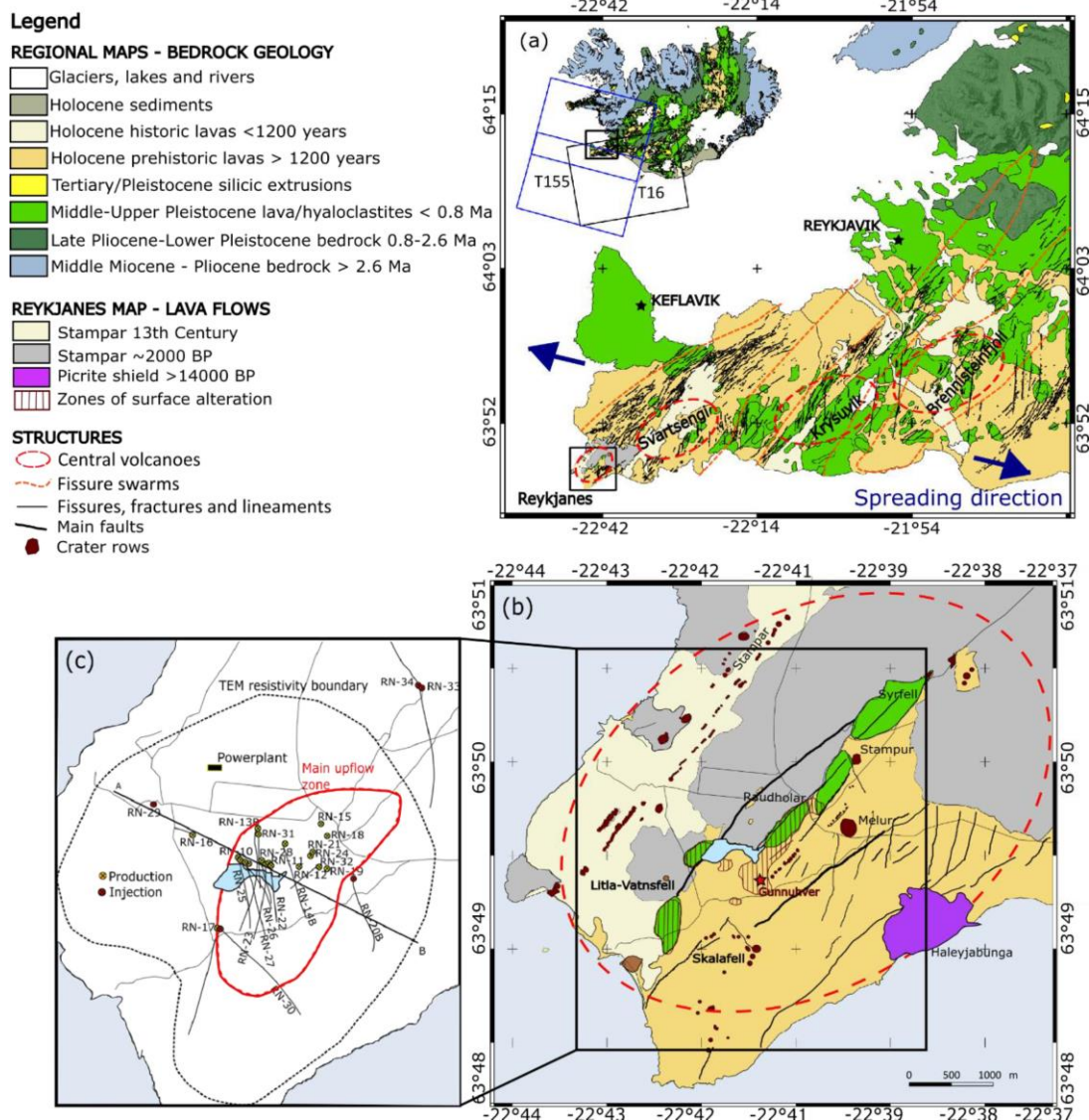


Figure 1. Geological maps. (a) Reykjanes Peninsula (Hjartarson and Saemundsson 2014), showing central volcanoes (red dashed lines) and the contours of the fissure swarms (orange dashed lines) after Johannesson and Saemundsson (1998), fault and fissures (black lines) and the direction of plate spreading (blue arrows) after Clifton and Schlische (2003). Inset shows the location of the map (black square) and the coverage of the Sentinel-1 ascending (T16) and descending (T155) tracks in Iceland. (b) Reykjanes geothermal system (after Saemundsson *et al.*, 2010) showing the youngest lava flows and crater rows (red features) west of the area of high surface alteration (after Friðleifsson *et al.*, 2018). (c) Map showing the location of drillholes (red and yellow circled crosses) and the ground surface traces of directionally drilled wells (black lines). Most of the wells are situated within the main upflow zone (red contour line) identified from resistivity surveys by Karlsdóttir and Vilhjálmsson (2014), centred on the Gunnhver thermal area, where the surface manifestation of hydrothermal activity is the highest. See legend for explanations of all symbols.

Geothermal production at Reykjanes was initiated in 1976 but the highest extraction rates were reached in 2006 when a new 100 MWe powerplant was commissioned. Up to 800 kg/s of fluid were extracted during the early production, resulting in a 3 MPa pressure drop at ~1600 m depth between May 2006 and May 2009 that increased boiling conditions in the reservoir (Fridriksson *et al.*, 2010). While the main feed zones at 1.9–2.3 km depth are still liquid dominated, those situated between 800 and 1200 m depth began to supply the wells with saturated steam in 2008 (Sigurdsson, 2010). That year, two relatively shallow wells, RN-27 and RN-28, were drilled in the central part of the system down to 1225 m and 960 m depth, respectively, to produce directly from this steam zone in the uppermost part of the reservoir (Fridriksson *et al.*, 2010). In 2018, 21.3 Mt of geothermal fluid were extracted by 15 deep production wells and the two shallow wells (Porvaldsson and Arnaldsson, 2017). Reinjection was initiated in 2009 at a rate of 15 kg/s to about 2.5 km depth to counterbalance pressure in the reservoir, and had continued to up to 5 wells at irregular rates, averaging to 75 kg/s during the 2009–2018 time period, with a maximum of 146 kg/s in 2016 (Fig. 2).

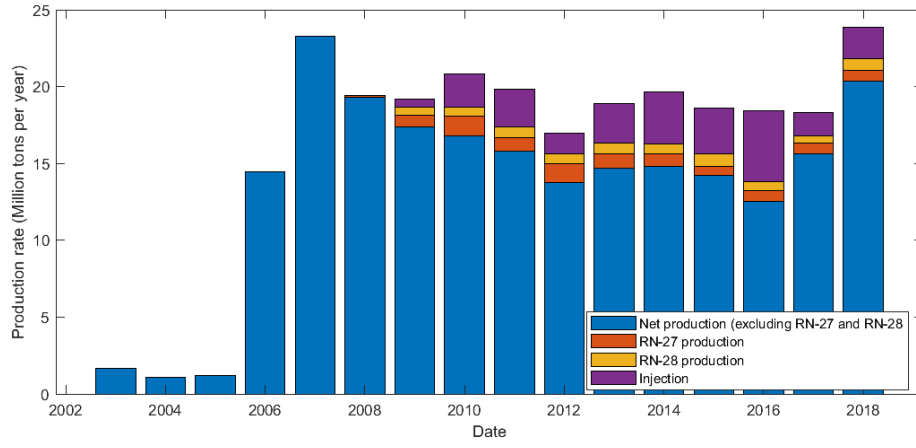


Figure 2: Net production rate (difference between extraction and injection rates) for all wells except shallow dry steam wells RN-27 and RN-28, extraction rates for RN-27 and RN-28 and injection rates for the period 2003-2018.

Monitoring of ground deformation started in Reykjanes before the commissioning of the new powerplant in 2006. Previous studies of deformation in this region include those undertaken by Keiding *et al.* (2010), Gunnarsson (2012), Michalczywska *et al.* (2014), Parks *et al.* (2018) and Receveur *et al.* (2019). Parks *et al.* (2018) undertook interferometric analysis of Envisat and TerraSAR-X data acquired between 2003 and 2016 to determine rates of displacement and provide constraints on the cumulative deformation field caused by utilization. Timeseries of displacement were extended in Receveur *et al.* (2018) with the use of Sentinel-1 satellite data spanning the 2015-2017 period, together with an analysis of the physical processes responsible for the observed deformation.

We here provide an update of the time series of deformation obtained from the InSAR analysis using Sentinel-1 images from March 2017 to May 2019 and evaluate deformation processes. We perform a probabilistic inversion of the Sentinel-1 data to determine the optimal parameters for the deformation source during the periods 2015-2019 and 2017-2019, using our best fit geometry configuration from earlier studies and compare the results with the production rates, pressure and temperature changes at depth, to infer the physical processing responsible for the deformation.

2. METHODS

2.1 InSAR analysis

Synthetic Aperture Radar (SAR) images of Reykjanes from the period 2003-2019 have been utilized to study ground motion over the geothermal reservoir. InSAR analysis determines the phase shift between SAR images acquired from approximately the same location overhead but at different times by forming interferograms (e.g. Liu *et al.*, 2017). As the satellite is “side-looking”, the relative displacement value of each pixel d_{LOS} in the interferogram is recorded as phase change, representing range change in the LOS direction towards the satellite proportional to the radar wavelength (e.g., Massonnet and Feigl 1998). In the absence of errors, it corresponds to the projection of the three-dimensional displacement field $\vec{d} = [d_E, d_N, d_{Up}]$ onto the unit vector $\vec{u} = [u_E, u_N, u_{Up}]$ pointing from the ground to the satellite (Eq. 1).

$$d_{LOS} = -\vec{d} \cdot \vec{u} \quad (1)$$

Ascending and descending interferograms covering the period 2003-2017 (Parks *et al.*, 2018; Receveur *et al.*, 2019) were formed from sets of images acquired over the study area by three different satellites. Data from the ENVISAT satellite covering the period 2003-2009 and from the TSX satellite covering the period 2009-2016 were processed using the DORIS software (Kampes and Usai, 1999). The STaMPS (Stanford Method for Persistent Scatterers) software (Hooper *et al.*, 2007) was used to generate independent time-series of displacement in the satellite's LOS for each period covered by the InSAR data and map the temporal evolution of deformation in the vicinity of the Reykjanes power plant (Parks *et al.*, 2018). For the period 2015-2017, Receveur *et al.* (2019) used data from the two C-band Sentinel-1A and 1B satellites launched by the European Space Agency in 2014 and 2016, respectively. Table 1 below summarizes the characteristics of each satellite and study period.

Satellite	Wavelength	Orbit	Track	Period covered	Total images	Heading	Average LOS vector
ENVISAT	C-band	Ascending	173	09/2005-08/2008	7	339°	[-0,319; -0,123; 0,940]
		Descending	138	2003-2009	24	201°	[0,395; -0,152; 0,906]
TSX	X-band	Ascending	26 s013	09/2009-2016	59	349°	[-0,670; -0,130; 0,731]
		Descending	110 s008	2009-2016	31	193°	[0,531; -0,123; 0,839]
SENTINEL-1	C-band	Ascending	16	08/2015-10/2017	40	-13°	[0,545; -0,123; 0,830]
		Descending	155	04/2015-10/2017	44	-169°	[-0,605; -0,123; 0,787]

Table 1. Summary of the characteristics of the satellites and images used for studies of ground deformation at Reykjanes in previous studies (Parks *et al.*, 2018; Receveur *et al.*, 2019)

In this study, we analyzed a total of 81 and 77 SAR images from Sentinel-1 ascending Track 16 (T16) and descending Track 155 (T155), respectively, acquired between January 2018 and May 2019. However, only 36 images from T16 and 27 images from T155 were retained for the final analysis, after removal of those significantly polluted by atmospheric noise, as judged by visual inspection. This set of images was processed jointly with the set of 2015-2017 Sentinel-1 images used in Receveur *et al.* (2019) (Table 1, Fig. 3) to generate an extended time series of deformation covering the October 2015 - May 2019 period, following the same approach.

Interferograms were formed using the InSAR Scientific Computing Environment (ISCE) software (Rosen *et al.*, 2015). The selected SAR images were co-registered to a single master image in each track, acquired on 20 August 2016 in T16 and 30 August 2016 in T155. For each track, average LOS velocity maps were generated over the Reykjanes area (Fig. 4). Displacement rates were determined for pixels having a coherence higher than 0.3 in each interferogram, as estimated by the ISCE software, using linear regression of the LOS displacement values within the whole set of interferograms in series. In addition, we created time series of LOS displacements for the average phase value of a set of pixels situated in the area of highest deformation of the ascending and descending velocity maps (Fig. 5). This approach was applied in order to reduce potential effects from individual pixels with significant noise.

In addition, we derive the vertical (“near-vertical”) n_V and the east (“near-east”) n_E component of the 2015-2019 deformation field (Fig. 4) using a linear combination of the LOS velocities measured in the ascending and descending tracks (see Receveur *et al.* (2019), and references therein). Those were used to estimate the cumulative displacement throughout the study period.

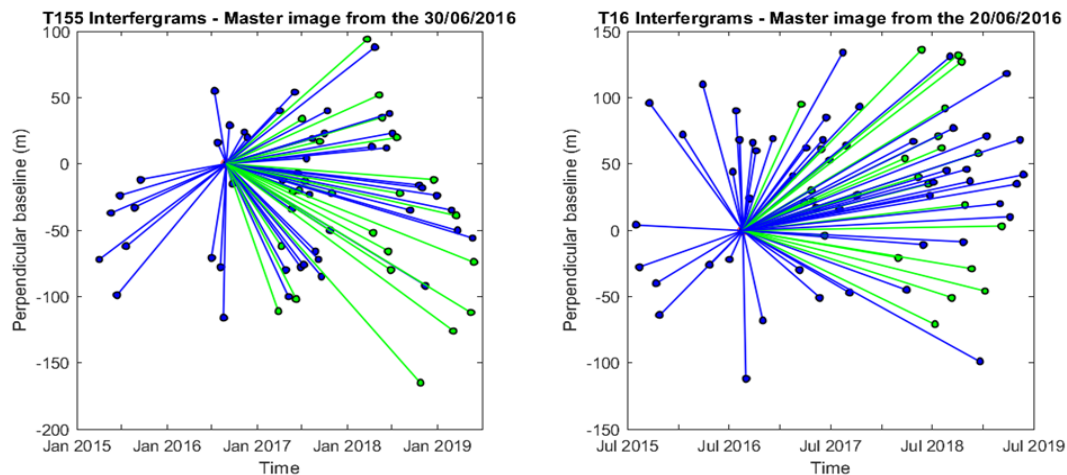


Figure 3. Star graphs showing the time interval and the distance between the locations of the satellite at the two acquisition times, in the direction perpendicular to the satellite viewing direction, of the interferograms used in the time-series and for the construction of the average velocity maps. Each dot corresponds to a single image from Sentinel-1A (in blue) and Sentinel-1B (in green) and each line represents an interferogram. A total of 70 and 75 interferograms have been formed from 71 T155 images (left-hand panel) and from 76 T16 images (right-hand panel), respectively.

2.2 Geodetic modeling

We invert the average LOS displacement rates obtained from the time series analyses to estimate the parameters of a contracting source at depth that best replicates the 2015-2019 observations. A set of models representing deformation sources embedded within a homogeneous, isotropic and uniform elastic half-space are considered. They are assumed to correspond to a part of (i.e. the steam zone) or the total volume of the geothermal reservoir that causes the observed deformation. For the periods 2005-2008 and 2009-2016, a point pressure source (Mogi, 1958) and an ellipsoid source (Yang *et al.*, 1988) representing the geothermal reservoir were considered (Parks *et al.*, 2018). For the period 2015-2017, a Mogi source as well as a spherical source (McTigue, 1987), a planar horizontal square sill with uniform closing (Okada, 1985) and a horizontal penny shaped crack (Fialko *et al.*, 2001) were tested (Receveur *et al.*, 2019). Here, InSAR data are inverted considering the best fitting sources for the 2015-2017 period: a penny shaped crack and a horizontal square sill model. Inversions are performed based on a Bayesian optimization approach, using both the Geodetic Bayesian Inversion Software (GBIS v1.0 ©2017 Marco Bagnardi), developed at the University of Leeds (Bagnardi and Hooper, 2017) and the modeling approach from Drouin *et al.* (2017), as explained in Receveur *et al.* (2019).

3. RESULTS

3.1 Background from previous studies

InSAR analysis from 2005 to 2016 (Parks *et al.*, 2018) showed that in the initial years of production (2005-2008 period), the LOS deformation signal at Reykjanes together with the near-vertical and near-east displacements are characterized by an elongated elliptical shape trending in the NE-SW direction. During the 2009-2016 period, velocity maps reveals that the highest LOS and near-vertical displacements are located in the center of a sub-circular deformation bowl centered on the well field. The near-east displacement was also more focused and characterized by contraction towards the center of the zone of highest deformation. Results for the 2015-2017 period covered by the Sentinel-1 data (Receveur *et al.*, 2019) indicated similar deformation pattern compared to the 2009-2016 one. This also confirmed the continuous decrease in the average rate of maximum subsidence measured in the most deforming area relative to the InSAR reference area situated to the east of the geothermal field. Using the near-vertical and near-east velocities derived for each time period (Table 2), a maximum cumulative subsidence and contraction of -0.289 m and 0.148 m, respectively, were inferred for the period June 2005 – October 2017.

Satellite	Orbit	Period	LOS rate (mm/yr)	Best-fitting model	Volume change	Near-vertical / Near east displacement
ENVISAT	Asc	18/06/2005-16/08/2008	-33	Yang	$-2.3 \times 10^6 \text{ m}^3$	-0.08 m
	Desc	16/06/2005-14/08/2008	-28			-0.07 m and + 0.07 m
TSX	Asc	29/09/2009-11/08/2016	-24	Mogi	$-1 \times 10^6 \text{ m}^3$	-0.19 m
	Desc	24/09/2009-17/08/2016	-21			-0.12 m and +0.06 m
TOTAL 2005-2016 (Parks <i>et al.</i> , 2018)						-0.260 m 0.140 m
Sentinel-1	Asc	02/08/2015-14/10/2017	-16	PSC / Sill	$-0.9 \times 10^5 \text{ m}^3/\text{yr}$	-25 mm/yr
	Desc	02/04/2015-30/10/2017	-20			-10 mm/yr and +5 mm/yr
TOTAL 2005-2017 (Receveur <i>et al.</i> , 2019)					$-3.8 \times 10^6 \text{ m}^3$	-0.289 m 0.148 m

Table 2. Summary of results from previous studies, including the LOS displacement rates, near-east and near-vertical velocities in areas of maximum deformation and volume changes of the best fitting deformation sources for each study period.

Inverse models for the 2005-2008 and 2009-2016 time period were performed using the cumulative LOS displacements obtained for each time period (Parks *et al.*, 2018). The optimal source for the period covering the ENVISAT observations (2005-2008) corresponds to a near-horizontal ellipsoidal source at about 2.2 km depth, displaying a volume change of $-2.3 \times 10^6 \text{ m}^3$. In the period spanning the TSX observations (2009-2016), results indicated a volume change of $-1.0 \times 10^6 \text{ m}^3$ for a best fitting point pressure source situated at about 1.2 km depth. This decrease in the rate of volume change (from $-7.3 \times 10^5 \text{ m}^3/\text{yr}$ in 2005-2008 to $-1.5 \times 10^5 \text{ m}^3/\text{yr}$ in 2009-2016) was confirmed by results obtained from the inversion of the average LOS displacement rates for the period 2015-2017, covered by the Sentinel-1 data. The best fit was there obtained for a penny shaped crack located at a depth of about 1.2 km, with a radius of 700 m and contracting by an amount of about $-0.9 \times 10^5 \text{ m}^3/\text{yr}$. For all time periods, the locations and the dimensions of the modeling sources suggest that the deformation originates from the area of maximum production, slightly to the southeast of the hottest part of the system and north of Gunnhver fumarole (Fig. 1).

3.2 InSAR results 2015-2019

LOS velocity maps for the whole 2015-2019 period reveal a relatively sub-circular deformation pattern centered on the geothermal field (Fig. 4), as observed during the 2015-2017 time period (Receveur *et al.*, 2019). Time-series analyses for the 2015-2019 period reveal an average maximum LOS rate of -20 mm/yr for Sentinel-1 T16 and -23 mm/yr for T155 in the assumed zones of maximum deformation, relative to the InSAR reference area. This reference area is situated near the STAD GPS station where a natural subsidence at a rate of about 6 mm/yr was measured before production began in 2006 (Hreinsdottir *et al.*, 2001). As subsidence of this station has continued at a similar rate after the production began, using this point as a reference allows us reducing the contribution of other natural deformation signals compared to those induced by geothermal utilization (Parks *et al.*, 2018).

We also performed independent linear regressions of the LOS displacements from interferograms for the 2015-2017 and 2018-2019 periods separately to identify potential variations between the two periods. For both tracks, we observe an increase in the LOS displacement rates, from -17 to -25 mm/yr for T16 and from -24 to -27 mm/yr for T155, for the 2015-2017 and the 2018-2019 time periods, respectively. This corresponds to an increase in the deformation rates of about 47% for T16 and 16% for T155 in the latest years relative to the 2015-2017 period (Fig. 5).

Results from the decomposition of the signal in near-vertical and near-east displacements show comparable patterns to the ones obtained for both the 2009-2016 and 2015-2017 periods (Parks *et al.*, 2018; Receveur *et al.*, 2019). The maximum near-vertical displacement rate, located in the central part of the subsidence bowl, is about -26 mm/yr relative to the InSAR reference area. The near-east displacement field is characterized by a contraction towards the center of this zone of highest deformation, with an eastward displacement of about 7 mm/yr of the western part of the field and a westward motion of about -11 mm/yr of the easternmost part. Details for the periods 2015-2017 and 2018-2019 are summarized in Table 3. As shown in Fig. 6, the highest rates of LOS displacement in the area of maximum change were observed during the first 2–3 years of production (Parks *et al.*, 2018), followed by an exponential decrease between 2008 and 2017. Based on the average 2015-2019 near-vertical and near-east velocities of -26 and 9 mm/yr, and on the values of cumulative subsidence and contraction in August 2016 estimated by Parks *et al.* (2018), we infer a cumulative subsidence of -0.332 m and a total contraction of 0.165 m for the whole period June 2005-May 2019.

Results for the 2018-2019 period are more uncertain than those for the 2015-2017 period, due to the lower coherence in the area of maximum deformation in the interferograms during this period (higher perpendicular baseline, with a maximum of -165 m for the T155 2016 August 30–2018 October 25 interferogram). However, the analysis of Sentinel-1 data in the 2018-2019 period data suggests an increase in the contraction and subsidence rates compared to the 2015-2017 period, in accordance with the increased LOS displacement rates observed in 2018-2019 (Fig. 5).

Based on these results, we perform inversions of the Sentinel-1 InSAR data for the periods 2015-2019 and 2018-2019 to determine the location and the volume change of the best-fitting deforming sources at depth during those time periods.

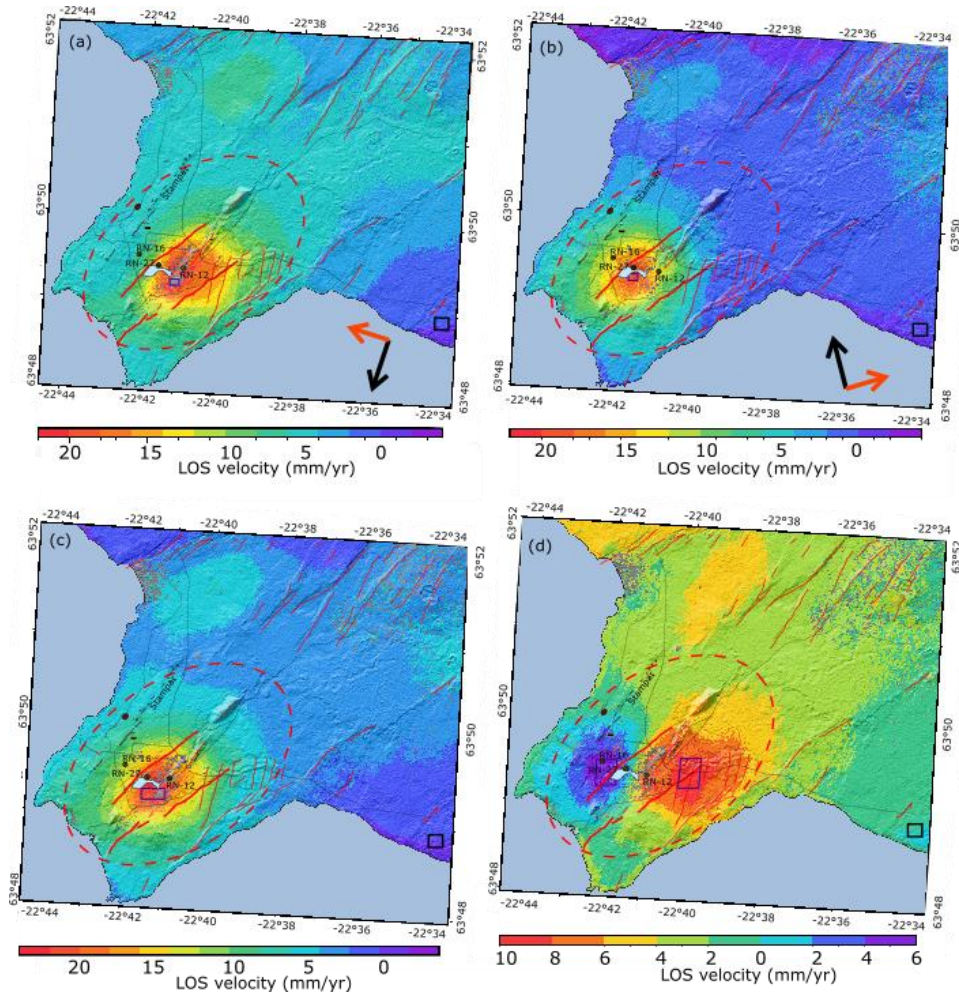


Figure 4. (a) LOS velocities for T155 and (b) LOS velocities for T16. (c) Estimated near-vertical and (d) near-east horizontal velocities; in mm/yr, for the period 2015-2019. The grey color indicates areas with coherence < 0.3 in all interferograms in the timeseries. The black square corresponds to the reference area and the dark blue squares correspond to the sampling areas for the estimation of the average displacement rates. Sampling areas contain 218 pixels with coherence > 0.3 in T16, 160 in T155, 637 in the near-vertical velocity maps, and 1769 and 2201 pixels in the western and eastern zones of the near-east velocity maps, respectively. The red dashed circle indicates the location of the Reykjanes system, the thin red lines represent the faults of the fissure swarm (Clifton and Schlische, 2003) and the bold red lines correspond to the Litla-Vatnsfell and Skalafell faults.

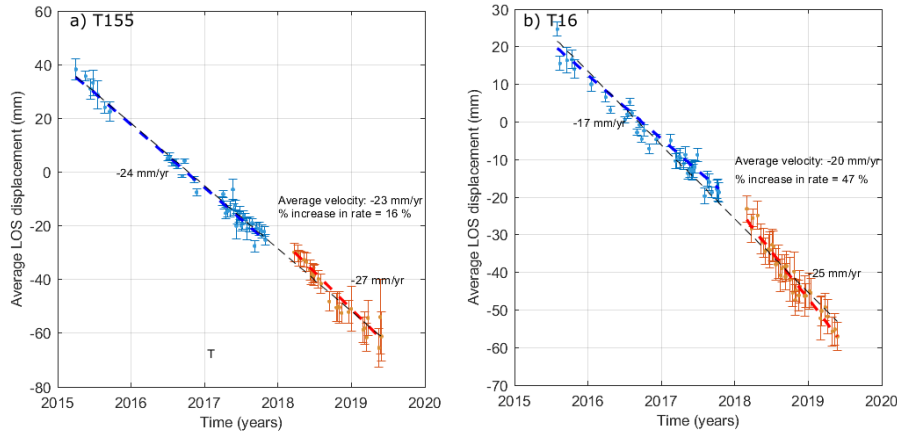


Figure 5. Time-series analysis of the average displacement of a set of points situated in the middle of the most deforming area, for pixels having a coherence > 0.3 in the selected interferograms. Error bars represent the uncertainty in the average displacement. Dashed lines correspond to linear rates for the different periods. Due to the lack of pixels in the area of maximum deformations in the 2018-2019 periods, the selected areas for determining the average LOS rates (dark blue squares in Fig. 4) have been modified compared to the study of Receveur *et al.* (2019), which explains the differences in the average 2015-2017 velocities given in Table 2. (a) Average LOS change of pixels within the area (-22.687°E ; -22.683°E ; 63.820°N ; 63.821°N) for T155 relative to a master image acquired on the 30 August 2016 (Fig. 4a). (b) Average LOS change of pixels within the area (-22.693°E ; -22.689°E ; 63.823°N) for T16 relative to a master image acquired on the 20 August 2016 (Fig. 4b).

Satellite	Track	Period	LOS Rate (mm/yr)	Near-vertical / Near-east velocities (mm/yr)
Sentinel-1 2015-2019	Asc	02/08/2015-25/05/2019	-20	-26
	Desc	02/04/2015-29/05/2019	-23	-11 and +7
Sentinel-1 2015-2017	Asc	02/08/2015-14/10/2017	-17	-27
	Desc	02/04/2015-30/10/2017	-24	-12 and +6
Sentinel-1 2018-2019	Asc	01/03/2018-25/05/2019	-25	-26
	Desc	23/03/2018-29/05/2019	-27	-13 and +11

Table 3. Summary of the average LOS, near-vertical and near-east displacement rates in the areas of maximum deformation. Pixels in the near-vertical velocity map (Fig. 4c) are selected within the area (-22.693°E; -22.683°E; 63.820°N; 63.822°N). Eastward and westward displacements are sampled within the areas (-22.704°E; -22.695°E; 63.821°N; 63.826°N) and (-22.668°N; -22.659°N; 63.821°N; 63.827°N), respectively, in the near-east velocity map (Fig. 4d).

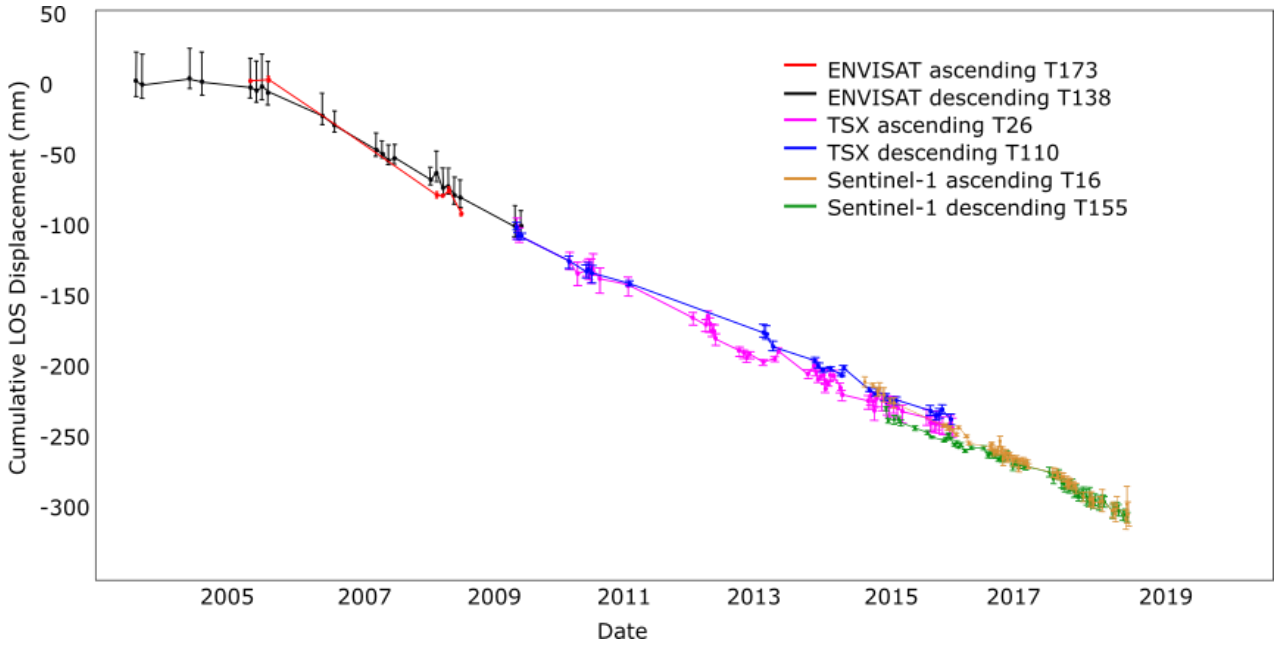


Figure 6. Time series of line-of-sight (LOS) displacement for the whole period 2003-2019 with error bars. The displacement time series displays the difference between two reference areas. ENVISAT and TSX time series are from Parks *et al.* (2018).

3.3 Models

In this study, we performed inversion considering the best fitting sources for the 2015-2017 period: a penny shaped crack (PSC) and a horizontal square layer horizontal sill (Receveur *et al.*, 2019). LOS velocity maps subsampled in a regular grid of $0.002^\circ \times 0.001^\circ$ in longitude and latitude were used as input for the sill model, inverted using the approach of Drouin *et al.* (2017) and described in Receveur *et al.* (2019). Inversion for the PSC model were performed using the GBIS software, using jointly the T16 and T155 velocity maps subsampled using a Quadtree approach. In both approaches, LOS velocities are inverted relative to the point (-22.564°E; 63.814°N) located close to the reference area for the InSAR maps. Modeling results are summarized in Table 4.

	2015-2019		2018-2019	
	PSC	Sill	PSC	Sill
Number of data point T16/T155	172 / 170	3123 / 2817	143 / 263	3296 / 3036
Longitude	-22.687 ^{-22.686} _{-22.687}	-22.687 ^{-22.657} _{-22.705}	-22.688 ^{-22.687} _{-22.688}	-22.688 ^{-22.656} _{-22.708}
Latitude	63.820 ^{63.820} _{63.819}	63.822 ^{63.827} _{63.811}	63.819 ^{63.819} _{63.819}	63.823 ^{63.827} _{63.812}
Depth	-1436 ⁻¹³²⁷ ₋₁₅₂₂	-1790 ⁻⁸⁸² ₋₂₁₆₃	-1205 ⁻¹¹¹⁴ ₋₁₂₉₆	-1788 ⁻⁸⁰⁸ ₋₂₁₆₄
Radius a (m)	245 ⁴¹⁸ ₂₂₂		221 ³⁰⁰ ₂₂₀	
Size (m)		608 ¹⁸⁰⁷ ₄₀₀		608 ¹⁷⁴² ₄₀₀
Δh (m/yr)		-0.19 ^{-0.03} _{-0.81}		-0.21 ^{-0.03} _{-0.78}
$\Delta P/\mu$ ($\times 10^{-3}$)	-2.8 ^{-0.6} _{-3.9}		-3.2 ^{-1.0} _{-3.3}	
ΔV ($\times 10^5$) (m ³ /yr)	-0.83 ^{-0.82} _{-0.86}	-0.97 ^{-0.70} _{-1.30}	-0.69 ^{-0.68} _{-0.73}	-0.91 ^{-0.77} _{-1.25}

Table 4. Modeling results for the sill model obtained from the approach from Drouin *et al.* (2017) and for the penny shaped crack (PSC), Mogi and Yang models, using the GBIS software, for the periods 2015-2019 and 2018-2019. Δh is the opening rate, $\Delta P/\mu$ the ratio of pressure change to shear modulus and ΔV the volume change of the modeling sources.

Modeling results for both the PSC and sill model indicate a source contracting by about $-0.9 \pm 0.1 \times 10^5 \text{ m}^3/\text{yr}$ in the 2015-2019 period. The volume change for the PSC is estimated from equation 2.

$$\frac{\Delta P}{\mu} = \frac{\Delta V}{2a^3} \quad (2)$$

with $\Delta P/\mu$, ΔV and a , the ratio of pressure change to the shear modulus, the volume change of the source and its radius, respectively.

This is in accordance with the results obtained for the 2015-2017 period (Receveur *et al.*, 2019) and confirms the continuation of the contraction of a deforming source at a near constant rate since 2015, and at a similar location. However, results for both models reveal a source of smaller size, with the radius of the best fitting PSC representing about 1/3 of its 2015-2017 radius, and the length of the sill source reaching half of its 2015-2017 size.

Independent results for the period 2018-2019 (Fig. 7) suggest no significant changes in the location and characteristics of the deforming sources with respect to results for the whole 2015-2019 period (Table 4). The rate of volume change is indeed maintained to $(0.7-0.9) \times 10^5 \text{ m}^3/\text{yr}$ for both models. In the PSC model, a higher $\Delta P/\mu$ ratio (-3.0×10^{-3} against -9.9×10^{-5} in 2015-2017) allows compensating for the smaller size and slightly deeper location of the deforming source. The greatest changes are however observed for the best fitting sill model, that reveals a greater closing rate ($\sim 20 \text{ cm/yr}$ against 4 cm/yr in 2015-2017) of a source originating from about 600 m deeper than in 2015-2017 (about 1.8 km), contrasting well with the depth of the best fitting PSC (1.2 km).

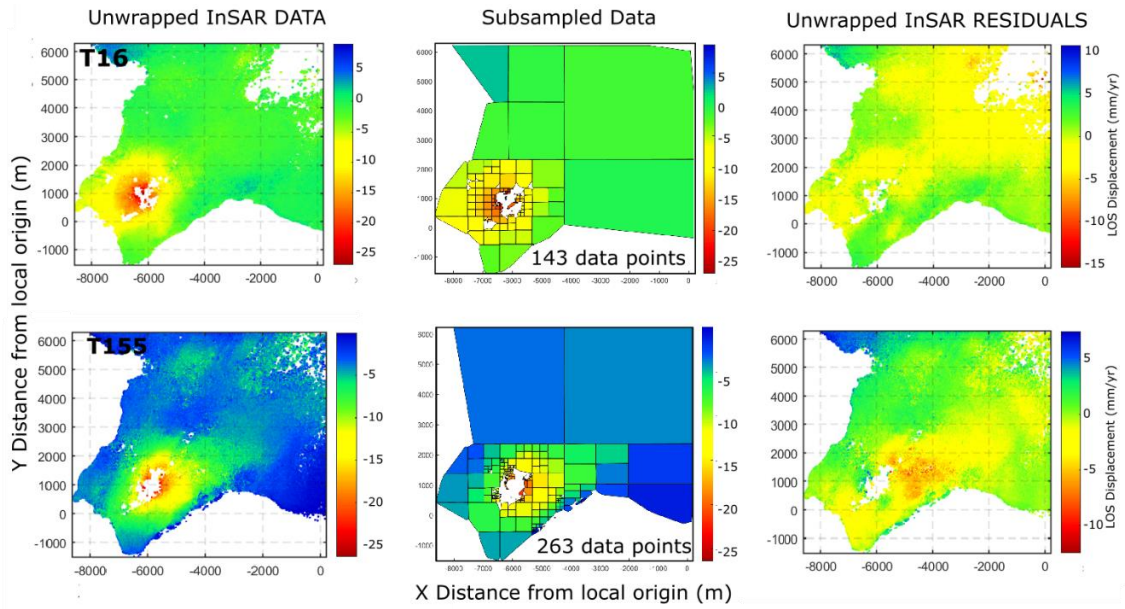


Figure 7. Data, model predictions and residuals for the 2018-2019 penny shaped crack modeling source, for track T16 (upper row) and T115 (lower row).

Modeling results for the 2015-2019 period thus indicate a similar volumetric contraction rate of the source as in the years since 2009 (Parks *et al.*, 2018, Receveur *et al.*, 2019). This is somewhat surprising, considering the higher rates of deformation in the central part of the deformation field (Fig. 5). The variability in the depth of the best fitting sources in 2018-2019 (i.e. 1.2 km for the PSC and 1.8 km for the sill source) suggests that deformation during this time interval is more complex and cannot be fully explained by one single shallow source. However, results must be considered with caution, as the wide confidence intervals for the best-fitting model parameters (Table 4) shows that results are quite uncertain, probably due to the lower coherence of the input InSAR data.

4. DISCUSSION: RELATIONSHIP BETWEEN DEFORMATION AND PHYSICAL PROCESSES

Ground deformation above geothermal reservoirs is often attributed to poro-elastic or thermo-elastic processes, associated with pressure change or cooling of the reservoir rock. Change in specific volume, v , relates to change in pressure, P , and temperature, T , through the following equation:

$$dv = \left(\frac{dv}{dT}\right) dT + \left(\frac{dv}{dP}\right) dP = v\alpha_v dT - vcdP \quad (3)$$

where α_v is the volumetric coefficient of thermal expansion and c the compressibility of the fluid saturated material. In a liquid-dominated system, a decrease in pore pressure dP resulting from the depletion of fluid storage may lead to the compaction of water bearing deposits due to increasing effective stress (Grant and Bixley, 2011; Terzaghi, 1925). Cooling of the rock matrix under natural recharge or the reinjection of cooler fluid can also induce volumetric contraction. Vaporization processes, which require the transfer of heat energy from the rock to the fluid may also lead to cooling in two-phase systems (e.g. Im *et al.*, 2017, Ali *et al.*, 2016). Although the effects of pressure drop are generally dominant at the beginning of geothermal utilization, Im *et al.* (2017) suggested that thermal contraction may become the main driver of deformation in geothermal reservoir, taking over poro-elastic compaction when steady state pressure conditions are reached after a few years of production (Mossop and Segall, 1997). Thermal and poro-mechanical processes are however generally coupled in two-phase systems and can occur on various time scales.

To better understand the processes responsible for the deformation at Reykjanes, Receveur *et al.* (2019) compared the inferred depth of the best fitting deformation source for the different time periods with geological, temperature and pressure profiles, together with an analysis of the production history of the reservoir. That study inferred a migration of the modeled source of deformation from 2.2 km depth in 2006-2009 to 1-1.4 km depth in 2009-2017 together with the change in both the subsidence pattern and the deformation rate since the end of 2008 was connected to the development of a steam zone in the uppermost part of the reservoir (between 600 and 1200 m depth). The pattern of the decline in the rate of volume change of the best fitting sources correlated well with the decrease in the rate of pressure drop measured at 1625 m b.s.l in the liquid dominated part of the reservoir until end of 2015 (from about -0.5 MPa/year in 2003-2009 to -0.1 MPa/year in 2009-2015). During the initial 2003-2009 period, both the shape of the best fitting deformation source (i.e. the ellipsoid) and the deformation pattern obtained from InSAR analysis seems to coincide well with the alignment of the NE-SW striking fissure swarm at Reykjanes. It was therefore suggested that the deformation was related to the compaction of deep basaltic rocks and dolerites in response to the large 3.0 MPa pressure drop and its diffusion in the central part of the reservoir along deep permeable NE-SW striking faults.

In 2015, a pressure decrease cumulating up to -3.8 MPa was measured at 1625 m.b.s.l relative to 2005. Between 2015 and 2017, pressure however increased by about 0.15 MPa/yr at that depth in well RN-12, while a continued pressure decline at a rate up to -0.2 MPa/yr was measured at 925 m b.s.l. in the upper steam dominated part of the reservoir, resulting in an additional pressure drawdown of about -1.7 MPa between 2009 and 2017 when compared to the observations at 1625 m b.s.l. (Fig. 8). Moreover, despite no significant temperature change has been measured in the convective zone (below 1500 m depth) since production started, cooling at an average rate of 4-5 °C/year had been suggested close to and within the steam zone in the 2009-2015 period, based on the monitored temperature in shallow wells RN-27 and RN-28 (Guðmundsdóttir, 2016). The continued subsidence but at lower rate since 2009 was therefore attributed to processes within the 400 m thick steam zone, including compaction within the inferred shallow steam zone of higher compressibility (about one order of magnitude higher than in the liquid dominated part of the reservoir, as estimated in Receveur *et al.*, 2019) and thermal contraction of the reservoir rock. The lateral extent of the modeled depressurized sources in 2015-2017 indicates that this steam zone covers a surface area of about 2 km², in accordance with the extent of the geothermal manifestation on surface (Palmason *et al.*, 1985).

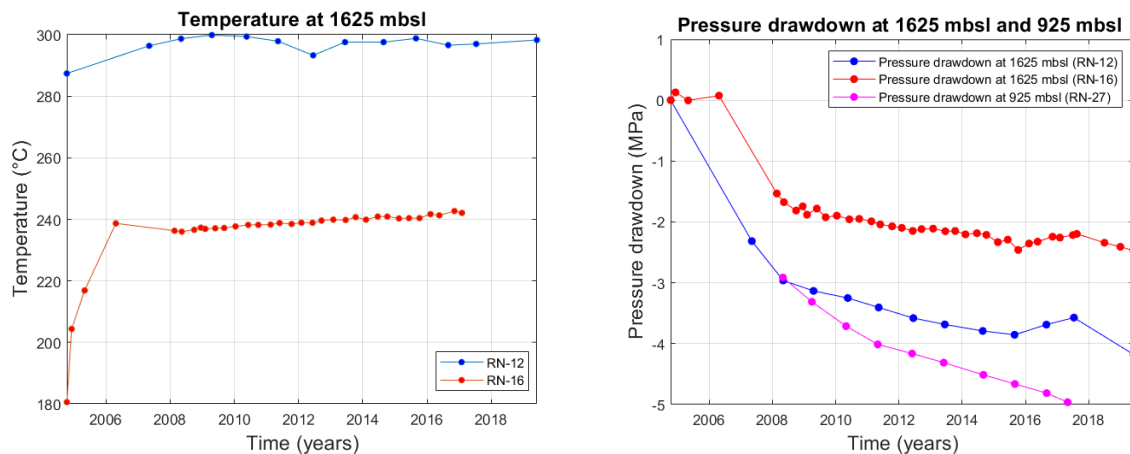


Figure 8. Pressure and temperature monitoring in the production well RN-12 situated in the center of the well field and the observation well RN-16 situated at the periphery, at 1625 m.b.s.l., together with pressure change in well RN-27 (925 m.b.s.l.)

Since the beginning of 2018, renewed pressure decline has been inferred at 1625 m.b.s.l, reaching -0.15 MPa/yr in well RN-16 and -0.32 MPa/yr in well RN-12 (Fig. 8). This new decline is inferred to result from the significant increase in the net extraction rate, from 437 kg/s in 2016 to 722 kg/s in 2018, partly explained by a decrease in reinjection rates from 146 kg/s in 2016 to 50 kg/s in 2017 (Fig. 2). Values of pressure and temperature changes at 900 m.b.s.l are not available for the period 2017-2019. However, one suggests that the pressure decline measured at 1625 m.b.s.l might be favorable to the development of boiling conditions in the reservoir and to the vaporization of liquid geothermal fluid. Such conditions were indeed already observed during the initial 2-3 years of geothermal utilization at Reykjanes, leading to the development of the steam zone. We can thus expect similar processes during the period 2018-2019. After a reduction of steam recharge and/or the condensation of steam during the period 2015-2017 linked to both the increase in the extraction of steam directly from the steam zone in 2009-2016 and the increase in reinjection rate until February 2017, changes in the production strategy would favor the recovery of steam from the end of 2017. The hypothesis of an enhanced steam recharge in the steam zone is moreover supported by the increase in the mass extraction rates for the shallow wells in 2018, especially for RN-28 that reaches its highest steam mass withdrawal of about 0.7 Million tons since 2015.

The increase in the maximum LOS, near-vertical and near-east displacement rates observed in the central part of the geothermal field in 2018-2019 seems to be in accordance with the new increase in the rate of pressure decline in the reservoir. However, despite no significant changes in the characteristics of the tested modeling sources have been detected throughout the 2015-2019 time period (i.e. X/Y location, volume change...), results for the sill source reveal a deformation originating from greater depth (~1.8 km) in 2018-2019 compared to 2015-2017. In addition, some residuals located NE from the main deformation zone in T155 (i.e. see PSC model in Fig. 7) and elongated in the NE-SW direction in the sill model indicate that all the deformation cannot be totally explained by one shallow or deep source. This may suggest that the deformation is changing and that a combination of shallow and deep processes may explain the subsidence observed from 2018. Other modeling sources, such as the rectangular dipping dyke (Okada, 1985) or a dipping ellipsoid (Yang *et al.*, 1988) might be able to explain those residuals and potentially infer the possible influence of the NE-SW faults of the fissure swarm. The smaller size of the modeling sources obtained in 2018-2019 may finally suggest that the geothermal reservoir has continued contracting, in accordance with the increased contraction rate measured in the InSAR data.

Based on our results, we suggest that a combination of shallow and deep processes might explain the deformation observed from 2018 at Reykjanes. The lack of consistency between the pressure decline measured at 1.6 km depth in 2018-2019 and the shallow depth of the best-fitting penny shaped crack (< 1.4 km) might be due to a potential delay before the effects of pressure decline at depth to be detected at a significant confidence level by surface geodetic methods. A combination of larger depth for the actual deformation source, the short period spanned since the pressure started to drop and the lower coherence in the 2018-2019 interferograms (i.e. lack of input data in the area of maximum deformation) would prevent precise estimates of the deformation rates and thus of the characteristics of the best-fitting deforming sources. Further monitoring of pressure/temperature changes and additional modelling work are therefore needed to understand the processes occurring in the reservoir since 2018.

4. CONCLUSION

Ground deformation at the Reykjanes geothermal area during the 2015-2019 has been constrained by interferometric analysis of Sentinel-1A and 1B radar images. LOS changes average to about 22 mm/yr in the satellite LOS in the selected area of maximum deformation in both ascending and descending satellite tracks. When results from the two tracks are combined, the observations reveal a subsidence bowl centered on the well field together with a horizontal contraction toward the center of the deforming area, as observed since 2009. In the initial years of production, the wider deformation at Reykjanes suggested that the initial high pressure drop measured between 2006 and 2008 in the geothermal system influenced a wider volume, bracketed by the boundaries of the Reykjanes fissure swarm, elongated in the same manner as the displacement signal. After 2009, less crustal volume has been responsible for the observed changes, attributed to more localized processes in the reservoir over time and a change in the deformation mechanisms. Between 2006 and 2009, deformation has been explained by the compaction of deep reservoir rocks favored by pressure diffusion along the NE-SW faults, while deformation between 2009 and 2017 was attributed to combined poro- and thermo-elastic processes within a steam zone located in the upper part of the reservoir.

Comparison of time-series analyses during the periods 2015-2017 and 2018-2019 indicate an increase in the LOS deformation rates during the latter period. In 2018-2019, near-vertical velocities reach -27 mm/yr in the center of the geothermal field together with contraction toward the area of maximum subsidence at a rate of about 9 mm/yr. This increase in deformation rate in the last year correlates well with a new pressure decline measured at 1.6 km depth, in response to an increased mass withdrawal since the beginning of 2018. However, the inferred rate of volume change of the best fitting penny shaped crack and Okada sill modeling source tested in this study appears to be constant throughout the 2015-2019 period. When modelled as a penny shaped crack, a depth of about 1.2-1.4 km is found, in accordance with results for the 2015-2017 period. For a best fitting sill source, a greater depth of about 1.8 km is indicated. The disparities in the best-fitting sources depth together suggest that deformation during the 2018-2019 period is somehow more complex and cannot be fully explained by one single shallow source. Further monitoring and research are therefore required to model properly the deformation above the Reykjanes geothermal system since 2018 and expressed in the InSAR data, and to understand the reservoir processes responsible for this deformation since the new 2018 increase in production.

REFERENCES

- Ali, S.T., Akerley, J., Baluyut, E.C., Cardiff, M., Devatzes, N.C., Feigl, K.L., Foxall, W., Fratta, D., Mellors, R.J., Spielman, P., Wang, H.F., and Zemach, E.: Time-series analysis of surface deformation at Bradys Hot Springs geothermal field (Nevada) using interferometric synthetic aperture radar, *Geothermics*, **61**, (2016), 114-120.
- Bagnardi, M., and Hooper, A.: 2017. Geodetic Bayesian Inversion Software (GBIS, ver. 1.0), Centre for Observation and Modelling of Earthquakes, Volcanoes and Tectonics (COMET), University of Leeds, England (2017). Available at: <http://comet.nerc.ac.uk/gbis/>, last accessed 1 July 2019.
- Björnsson, S., Arnorsson, S., and Tomasson, J.: Exploration of the Reykjanes thermal brine area, Iceland, *Geothermics*, **2**(2), (1970), 1640-1650.
- Clifton, A. and Schlische, R.W.: Fracture populations on the Reykjanes Peninsula, Iceland: Comparison with experimental clay models of oblique rifting, *J. geophys. Res.*, (2003), **108**(B2), 2074, pp.17, doi:10.1029/2001JB000635
- Drouin, V., Sigmundsson, F., Verhagen, S., Ofeigsson, B.G., Spaans, K., and Hreinsdóttir, S.: Deformation at Krafla and Bjarnaflag geothermal areas, Northern Volcanic Zone of Iceland, 1993-2003, *J. Volcanol. Geotherm. Res.*, (2017), **344**, 92-105.
- Fialko, Y., Khazan, Y., and Simons, M.: Deformation due to a pressurized horizontal circular crack in an elastic half-space, with applications to volcano geodesy, *Geophys. J. Int.*, (2001), **146**, 181-190.
- Franzson, H., Thordarson, S., Björnsson, G., Gudlaugsson, S., Richter, B., Friðleifsson, G.Ó., and Thorhallsson, S.: Reykjanes high-temperature field, SW Iceland. Geology and hydrothermal alteration of well RN-10, *Proceedings*, Twenty-Seventh workshop on geothermal reservoir engineering, Stanford University, Stanford, California (2002).
- Franzson, H.: The high temperature system at Reykjanes, Iceland GeoSurvey report, ISOR-2004/012, (2004), pp. 68 (in Icelandic).
- Friðleifsson, G.Ó., and Richter, B.: The Geological Significance of Two IDDP-ICDP Spot Cores from the Reykjanes Geothermal Field, Iceland, *Proceedings*, World Geothermal Congress, Bali, Indonesia (2010). Also available at: www.iddp.is.
- Friðleifsson, G.Ó., Sigurdsson, Ó., Thorbjörnsson, D., Karlsdóttir, R., and Gilason, Th.: Preparation for drilling well IDDP-2 at Reykjanes, *Geothermics*, (2014), **49**, 119-126.
- Friðleifsson, G.O., Elders, W.A., Zierenberg, R.A., Fowler, A.P.G., Weisenberger, T.B., Mesfin, K.G., Sigurdsson, O., Albertsson, A.L., Nielsson, S., Einarsson, G., Óskarsson, F., Guðnason, E.A., Tulinius, H., Hokstad, K., Jóhannesson, Th., Benoit, G., Nono, F., Loggia, D., Parat, F., Cichy, S.B., Escobedo, D., and Mainprice, D.: The Iceland Deep Drilling Project at Reykjanes: Drilling into the root zone of an analog of a black smoker, *J. Volcanol. Geotherm. Res.*, (2018), pp. 19.
- Fridriksson, T., Oladottir, A.A., Jonsson, P., and Eyjolfssdóttir, E.: The response of the Reykjanes geothermal system to 100MWe Power production: fluid chemistry and surface activity, *Proceedings*, World Geothermal Congress, Bali, Indonesia (2010).

- Grant, M.A. and Bixley, P.F.: Geothermal reservoir engineering, 2nd edn., Academic Press, Burlington, USA (2011), pp. 378, ISBN: 978012383881.
- Guðmundsdóttir, V.: Svartsengi-Reykjanes. Reservoir Temperature and Pressure Monitoring, Iceland GeoSurvey report for HS-Orka, ÍSOR-2016/032 (2016), pp. 85 (Lokuð skýrsla).
- Guðnason, E.A., Arnaldsson, A., Axelsson, G., Berthet, J.C., Hallsorsdóttir, S., and Magnusson, I., T.: Analysis and Modeling of Gravity Changes in the Reykjanes Geothermal System in Iceland during 2004-2010, *Proceedings*, World Geothermal Congress, Melbourne, Australia (2015).
- Hjartarson, A. and Saemundsson, K.: Geological Map of Iceland. Bedrock, 1:600 000. Iceland GeoSurvey, Reykjavik, Iceland (2014).
- Hooper, A., Segall, P., and Zebker, H.: Persistent scatterer interferometric synthetic aperture radar for crustal deformation analysis, with application to Volcán Alcedo, Galápagos, *J. Geophys. Res. Solid Earth*, (2007), **112**(B7).
- Hreinsdóttir, S., and Einarsson, P.: Crustal deformation at the oblique spreading Reykjanes Peninsula, SW Iceland: GPS measurements from 1993 to 1998, *J. geophys. Res.*, (2001), **106**(B7), 803-816.
- Im, K., Elsworth, D., Guglielmi, Y., and Mattioli, G.S.: Geodetic imaging of thermal deformation in geothermal reservoirs: production, depletion and fault reactivation, *J. Volcanol. Geotherm. Res.*, (2017), **338**, 79-91.
- Johannesson, H. and Saemundsson K.: Geological Map of Iceland, 1:500 000. Tectonics., 1st edn., Icelandic Institute of Natural History, Reykjavik, Iceland (1998).
- Kampes, B., and Usai, S.: Doris: the delft object-oriented radar interferometric software, 2nd International Symposium on Operationalization of Remote Sensing, Enschede, the Netherlands (1999), **16**, pp. 20.
- Karlsdóttir, R. and Vilhjálmsson, A.M.: Reykjanes Geothermal Area, Southwest Iceland. Extension of 3D Inversion of MT Data, Iceland GeoSurvey report, ÍSOR-2014/016 (2014), pp. 134.
- Keiding, M., Arnadóttir, T., Jonsson, S., Decriem, J., and Hooper, A.: Plate boundary deformation and man-made subsidence around geothermal fields on the Reykjanes Peninsula, Iceland, *J. Volcanol. Geotherm. Res.*, (2014), **194**(4) 139-149.
- Liu, F., Fu, P., Mellors, R.J., Plummer, M., Ali, S.T., Reinisch, E.C., Liu, Q., and Feigl, K.L.: Inferring geothermal reservoir processes at the Raft River Geothermal Field, Idaho, USA through modeling InSAR-measured surface deformation, *Proceedings*, 42nd Workshop on Geothermal Reservoir Engineering, Stanford University, Stanford, California (2017).
- McTigue, D.F.: Elastic stress and deformation near a finite spherical magma body: Resolution of the point source paradox, *J. geophys. Res. Sol. Earth*, (1987), **92**(B12), 931-940.
- Massonnet, D., and Feigl, K.L.: Radar interferometry and its application to changes in the Earth's surface, *Geophysics*, (1998), **36**(4), 441-500. doi:10.1029/97RG03139
- Michalczevska, K., Hreinsdóttir, S., Dumont, S., and Sigmundsson, F.: Crustal deformation on the Western Reykjanes Peninsula 2009 to 2014 mapped by InSAR and GPS measurements, Institute of Earth Sciences report, JH1401, University of Iceland (2014), pp. 71.
- Mogi, K.: Relations between the eruptions of various volcanoes and the deformations of the ground surfaces around them, *Bull. Earthquake Res. Institute, Tokyo*, (1958), **36**, 99-134.
- Mossop, A., and Segall, P.: Subsidence at the Geysers geothermal field N. California from a comparison of GPS and leveling surveys, *Geophys. Res. Lett.*, (1997), **24**(14), 1839-1842.
- Okada, Y.: Surface deformation due to shear and tensile faults in a half-space, *Bull. Seism. Soc. Am*, (1985), **75**, 1135-1154.
- Palmason, G., Johnsen, G.V., Torfason, H., Saemundsson, K., Ragnars, K., Haraldsson, G.I., and Halldorsson G.K.: Assessment of geothermal energy in Iceland, National Energy Authority, Report OS-85076/JHD-10 (1985), pp. 134 (in icelandic).
- Parks, M., Sigmundsson, F., Sigurdsson, O., Hopper, A., Hreinsdóttir, S., Ófeigsson, B., and Ófeigsson, K.: Deformation due to geothermal exploitation at Reykjanes, Iceland, *J. Volcanol. Geotherm. Res.*, (2018), pp 12.
- Receveur, M., Sigmundsson, F., Drouin V., and Parks, M.: Ground deformation due to steam cap processes at Reykjanes, SW-Iceland: effects of geothermal exploitation inferred from interferometric analysis of Sentinel-1 images 2015-2017, *Geophys. J. Int.* (2019), **216**, 2183-2212. doi: 10.1093/gji/ggy540
- Rosen, P., Gurrola, E., Agram, P., Lavaller, M., and Powell, M.: ISCE Tutorial, NASA Jet Propulsion Lab., California Institute of Technology, CA, USA (2015), pp. 214.
- Saemundsson K., Johannesson, H., Hjartarson, A., Kristinnsson, S.G., and Sigurgeirsson, M.A.: Geological Map of Southwest Iceland, 1:100 000. Iceland GeoSurvey, Reykjavik, Iceland (2010).
- Sigurdsson, Ó.: The Reykjanes Seawater Geothermal System: it's exploitation under regulatory constraints, *Proceedings*, World Geothermal Congress, Bali, Indonesia (2010).
- Terzaghi, K.: Erdbaumechanik auf Bodenphysikalischer Grundlage. Franz Deuticke, Liepzig-Vienna (1925).
- Þorvaldsson, L., and Arnaldsson, A.: Svartsengi-Reykjanes. Vinnslueftirlit fyrir árið 2016, Vatnaskil report for HS Orka (2017), pp. 54 (in icelandic).
- Yang, X.M., Davis, P.M., and Dieterich, J.H.: Deformation from inflation of a dipping finite prolate spheroid in an elastic half-space as a model for volcanic stressing, *J. Geophys. Res. Solid Earth*, (1988), **93**(B5), 4249-4257.